Framework for autonomous navigation for a permanent resident aquaculture net grooming robot

Martin Skaldebø[1,*] Sveinung J. Ohrem[1] Herman B. Amundsen[1] Eleni Kelasidi[1] Nina Bloecher[1]

***Abstract*—This paper proposes methods to enable autonomous operation, specifically for localization and motion planning, of net grooming robots in aquaculture net pens and validates the proposed methods in both simulations and experimental fieldwork. Moreover, this paper suggests enabling uninterrupted operation by investigating the use of data from an inertial measurements unit that is a common sensor in underwater vehicles, rather than investing and upgrading to costly sensory systems that often require additional installation and calibration. In particular, the presented work consists of a localization method capable of estimating a robotic system's cylindrical position in an aquaculture net pen, a 3 DOF cylindrical robotic model, a method for path planning and collision avoidance, and a heading guidance and control system. The simulations demonstrate successful localization of the robotic system, while simultaneously planning and following collision-free trajectories in an environment obstructed by obstacles. Furthermore, the field trials successfully demonstrate that the system, when applied to net crawling robots, is capable of localization, path planning, and collision avoidance in an aquaculture setting. As follows, the presented work contributes to establishing net grooming robots as competitive candidates for biofouling management.**

***Index Terms*—Underwater robotics, aquaculture, net cleaning, collision avoidance**

I. Introduction

Biofouling, the undesired growth of organisms such as algae, mussels and hydroids on submerged marine structures, strongly impacts efficient and sustainable production in marine aquaculture [1]. The occlusion of the nets and the resulting increase in drag can cause deformation of the net and pen structure, increasing stress on mooring lines as well as restricting water flow. The latter can lead to decreased oxygen levels and increased risk for diseases and negative impacts on fish welfare [2].

In Norway, traditional biofouling management consists of regular (weekly to monthly) in-situ pressure washing of the net. This is conducted using large, self-propelled systems, or by using rigs attached to ROVs that are remotely operated from a service vessel. When cleaning from the inside of the pen, fouling organisms are removed from the net and released into the water column where they pose a risk to fish health and the spread of pathogens [1], [3]. If nets are impregnated with biocidal antifouling coatings containing e.g., copper, cleaning will also cause the increased release of harmful biocides into the environment [4]. Finally, as the operation is performed manually, it is limited by weather conditions that may subject operators to health and safety risks or force delays in service during adverse conditions [5], [6].

To avoid these disadvantages of traditional biofouling mitigation strategies, recent technological developments aim to establish autonomous net grooming as an alternative strategy for the aquaculture market. As opposed to the reactive removal of fouling organisms from nets, net grooming relies on continuous preventative treatment (i.e. brushing) of the net to forestall the establishment of fouling organisms and thus keep the net clean at all times [7], [8]. However, to be profitable and sustainable, net grooming needs to include autonomous, or at least automatic, capabilities [9]. Underwater localization, motion planning and control are essential functionalities that should be in place to solve such capabilities [10]. Current net grooming robots entering the Norwegian market include the Remora (Remora Robotics [7])), a net crawling robot that is attached to the net and moves on two crawl belts while brushing the net. As opposed to moving freely in the net pen, crawling on the net may simplify navigation, guidance and control algorithms as the number of degrees of freedom (DOF) needed to describe the robot's position can be reduced [11].

Autonomous navigation of robotic systems in aquaculture poses additional challenges compared to other marine industries, primarily due to the harsh and unstructured underwater environments with the attenuated nature of waves in water and constant change of net pen shape [12]. Moreover, localization of the robot in net cleaning operations is an important task in order to e.g. achieve autonomous navigation, plan cleaning operations, keep track of cleaning progress, and report observations. Therefore, determining the position of a robot relative to the net pen with ocean currents and waves impacting and deforming the net structure is a demanding task [13], [14].

This paper focuses on the development and demonstration of autonomous operations for a net crawling robotic system and proposes and validates a new method for localization of the robotic system in the net pen. The proposed localization method estimates the position of the robotic system in the net pen by utilizing the properties of the net, specifically the net dimensions, and depth and heading angle measurements from the robotic system. In addition, the paper proposes to

This work is supported by the Norwegian Research Council projects NetClean 24/7 [grant no. 296392] and CHANGE [grant no. 313737].

[1]SINTEF Ocean, Department of Aquaculture, Trondheim, Norway.

*Corresponding author: martin.skaldebo@sintef.no

use the elastic band method for path planning and collision avoidance, a method first presented in [15] and later adapted to a net-crawling robotic system described using cylindrical coordinates [16]. The elastic band method is used for planning a path for the continuous grooming of the net pen, while also avoiding obstacles that occur in the planned path by continuously performing re-planning. Note that the developed system is quite general and thus is applicable for any robot with similar degrees of freedom operating in a cylindrical or circular environment. The efficacy of the proposed methods has been demonstrated through simulations and through experiments in an industrial-scale fish farm.

This paper is structured as follows: Section II describes the robotic system including the robot model, localization, path planner and guidance system. Section III presents the results from simulations and experiments, and describes the experimental setup and the control system design. Concluding remarks and suggested future work are presented in Section IV.

II. Method

This section presents the implemented methods and describes the proposed localization method and the adapted elastic band method. In addition, the model of the robot and the guidance system used for experimental testing are presented.

A. Model of the robot

Modeling of the Remora robot was determined using the mathematical model of a net-crawling robot [11]. The Remora robot is attached to the net with hooked belts [7] and can be defined in a 3 DOF cylindrical coordinate system with the position vector

$$\bar{\boldsymbol{\eta}} = \begin{bmatrix} \alpha & D & \psi \end{bmatrix}^{\mathrm{T}}, \tag{1}$$

and the velocity vector of the robot defined as

$$\bar{\boldsymbol{\nu}} = \begin{bmatrix} u & r \end{bmatrix}^{\mathrm{T}}, \tag{2}$$

where α is the angular position, referred to as the azimuth angle, D is the Down coordinate in North-East-Down (NED) frame [17], ψ is the robot's heading angle, u is the robot surge speed relative to the assumed static net pen and r is the yaw rate. The equations of motion defined in [11] can then be described with

$$\dot{\bar{\boldsymbol{\eta}}} = \boldsymbol{J}_c(\psi)\bar{\boldsymbol{\nu}} \tag{3}$$

$$\dot{\bar{\boldsymbol{\nu}}} = \boldsymbol{M}_c^{-1}(-\boldsymbol{D}_{l,c}\bar{\boldsymbol{\nu}} - \boldsymbol{D}_{n,c}(\bar{\boldsymbol{\nu}})\bar{\boldsymbol{\nu}} + \boldsymbol{\tau}_c), \tag{4}$$

where $\boldsymbol{J}_c(\psi) \in \mathrm{R}^{3\times 2}$ is the transformation matrix between the body fixed reference frame and the cylindrical frame, $\boldsymbol{M}_c \in \mathrm{R}^{2\times 2}$ is the system inertia matrix, $\boldsymbol{D}_{l,c} \in \mathrm{R}^{2\times 2}$ and $\boldsymbol{D}_{n,c} \in \mathrm{R}^{2\times 2}$ are the linear and nonlinear damping matrices, respectively, and $\boldsymbol{\tau}_c \in \mathrm{R}^2$ is the control force and moment defined as

$$\boldsymbol{\tau}_c = \begin{bmatrix} \tau_u \\ \tau_r \end{bmatrix}, \tag{5}$$

where τ_u is the control force in surge and τ_r is the control moment in yaw. See [11] for more information and definitions of the individual matrices. The robot's position is in cylindrical coordinates and can be translated to the Cartesian NED frame with

$$N = r_c(t)\cos\alpha \tag{6}$$

$$E = r_c(t)\sin\alpha \tag{7}$$

$$D = D, \tag{8}$$

where $r_c(t)$ is the radius of the net pen at the current position of the robot. The radius may vary due to net deformation resulting from external forces and is therefore dependent on the position of the robot and the time. However, by assuming current speed < 0.3 m/s, the net deformation (volume reduction) is less than 10% [14]. Thus, the radius variation is considered to be negligible in this work and the radius can be considered as a static value r^*_c.

B. Localization Method

Global navigation satellite system (GNSS) signals are unable to penetrate water and hence cannot be used for underwater localization. Instead, other technologies may be applied. Localization of an underwater vehicle in a net pen using a Doppler Velocity Log (DVL) attached to the vehicle was tested in [18], where the measured length of the DVL beam vectors was used to approximate the geometry of a local region of a net pen in front of the vehicle. A similar approach using laser-camera triangulation instead of a DVL was presented in [19], displaying nearly as good signal quality, at less than 1/25th of the price. However, these solutions are not applicable for a vehicle attached to the net given that they consider the distance to the net as a principal measurement. Another, more general method includes the use of an ultra-short baseline (USBL) positioning system to measure the position of an underwater vehicle [20], although these systems can be costly and often require installation of an extra sensor on-board the robot. A method for estimating both the position of an underwater vehicle and the shape and position of a net pen was proposed in [21]. This method required acoustic sensors to be installed on both the vehicle and the net pen.

This paper proposes a simple, low-cost localization method utilizing readily available measurements, i.e., heading and depth measurements from the depth sensor and inertial measurement unit (IMU). Depth and IMU measurements are commonly available in most commercial underwater robotic systems.

The robotic system will operate in an aquaculture net pen, which can be assumed to have a cylindrical shape. The robotic system can therefore be localized by considering the depth and the angular position in the net pen as shown in Figure 1 [11]. Note that the angular position, referred to as the azimuth angle, can not be directly measured without the use of external sensors. Therefore, the developed localization method utilizes available measurements of the heading angle, ψ, and the depth, D, to estimate this azimuth angle, α. The method concerns a dead reckoning process that updates the

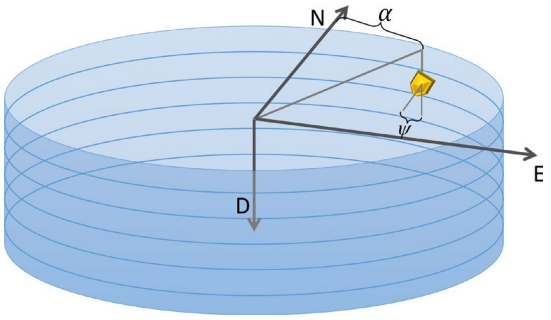

Fig. 1: Position of the robotic system in the net pen in North-East-Down (NED) frame and the azimuth angle and heading.

azimuth angle at each time step. The azimuth angle at a specific time step is determined by considering the azimuth angle and the vehicle heading angle from the previous time step in combination with the relative change in depth between the two time steps. Moreover, since the vehicle is attached to the net, it can be assumed that the vehicle's movement follows the net's geometry. The azimuth angle can be determined from the vehicle's position in a NED frame [17] with origin in the net pen center with

$$\alpha_i = \begin{cases} 3\pi/2 & \text{if } |N_i| < \epsilon_a \text{ and } E_i < 0 \\ \pi/2 & \text{if } |N_i| < \epsilon_a \text{ and } E_i > 0 \\ \tan^{-1}\frac{E}{N_i} & \text{otherwise,} \end{cases} \tag{9}$$

where α_i is the azimuth angle in the range $[0, 2\pi]$ at time step i and E_i and N_i are the East and North coordinates of the robot at time step i, respectively, and ϵ_a represents a small constant. The North and East coordinates are updated using a dead reckoning process that estimates the coordinates based on the position at the previous time step and the velocity between the previous and current time steps. The coordinates are updated with

$$N_i = N_{i-1} + u_{r,i}\cos(\alpha_{i-1})\sin(\psi_i)\Delta t_i, \tag{10}$$

$$E_i = E_{i-1} + u_{r,i}\sin(\alpha_{i-1})\sin(\psi_i)\Delta t_i, \tag{11}$$

where N_{i-1} and E_{i-1} are the North and East coordinates at time step $i-1$, respectively. Note that N_0 and E_0 have to be initialized at the start of any operation involving the dead reckoning process. Moreover, ψ_i is the heading angle of the vehicle in the range $[-\pi, \pi]$ at time step i, Δt_i is the amount of time between time step $i-1$ and time step i, and u_i is the vehicle's surge speed, calculated using

$$u_i = \begin{cases} \bar{u} & \text{if } |\psi| - \pi/2 < \epsilon_u \\ \frac{\Delta D_i}{\cos\psi_i} \frac{1}{\Delta t_i} & \text{otherwise,} \end{cases} \tag{12}$$

where $\bar{u}$ is the mean surge velocity, ϵ_u represents a small constant, and ΔD_i is the change in depth between time step $i-1$ and time step i, and $\Delta t > 0$ at all times. $\bar{u}$ is calculated from all previous time steps with

$$\bar{u} = \frac{1}{n}\sum_{i=1}^{n} u_i. \tag{13}$$

C. Elastic band method for path planning and collision avoidance

The elastic band method conceptualizes a path between the robot and a set of waypoints as a rubber band with partly overlapping bubbles that can be stretched to avoid obstacles and contracted to optimize the path [15]. The volumes within the bubbles represent subspaces of the vehicle's free space, and the size of the bubbles can be determined based on vehicle size, and proximity to obstacles. Based on the elastic band method originally presented in [15] and adapted to a net crawling robot in [16], the method can be divided into three distinct phases, where Phase 1 is conducted during the initialization of the path planner and Phases 2 and 3 at every time-step.

Phase 1 aims to produce an initial path of overlapping bubbles as the shortest path between a set of waypoints without considering any obstacles or other barriers.

Phase 2 deforms the path to achieve both optimality and collision avoidance by considering the internal contracting forces of the elastic band and repulsive forces from obstacles. Repulsive forces from the sea surface are also included to ensure that the planned path is in the feasible region below the sea surface, and attracting forces from the net pen to ensure that the path is constricted to the net surface.

Phase 3 ensures that the new trajectory is eligible by checking for redundant bubbles and ensuring that there is no gap between consecutive bubbles.

In this paper, the elastic band method is adapted to generate a collision-free trajectory along the net pen for a net-crawling robotic system. The robotic system does not contain any obstacle detection system, thus any obstacles that the system should evade are pre-programmed as virtual obstacles. Consequently, the elastic band planner receives waypoint positions, and obstacle positions as inputs and gives as outputs waypoints, including intermediate bubble waypoints, and the desired speed of the robotic system calculated by

$$u_d = \frac{r_b - r_{b,min}}{r_{b,max} - r_{b,min}}(u_{max} - u_{min}) + u_{min}, \tag{14}$$

where r_b is the radius of the first bubble and $r_{b,max}$ and $r_{b,min}$ are the maximum and minimum allowed bubble radius, respectively. Furthermore, u_{max} and u_{min} are the maximum and minimum surge speed, respectively. Letting the sizes of the bubbles dictate the desired speed of the robot relates the vehicle motion with the free space; e.g., the robot will move slower when in close proximity to obstacles compared to when there is little risk of collisions.

D. Heading Guidance

The output of the elastic band planner is the next waypoint that the robotic system should reach, defined by a depth and azimuth angle. In order to achieve this, a heading guidance is implemented based on the pure pursuit guidance with lookahead-based steering from [17]. The guidance system outputs a heading reference calculated by

$$\psi_r = \text{atan2}(\tilde{\alpha} r_c^*, \tilde{D}) \tag{15}$$

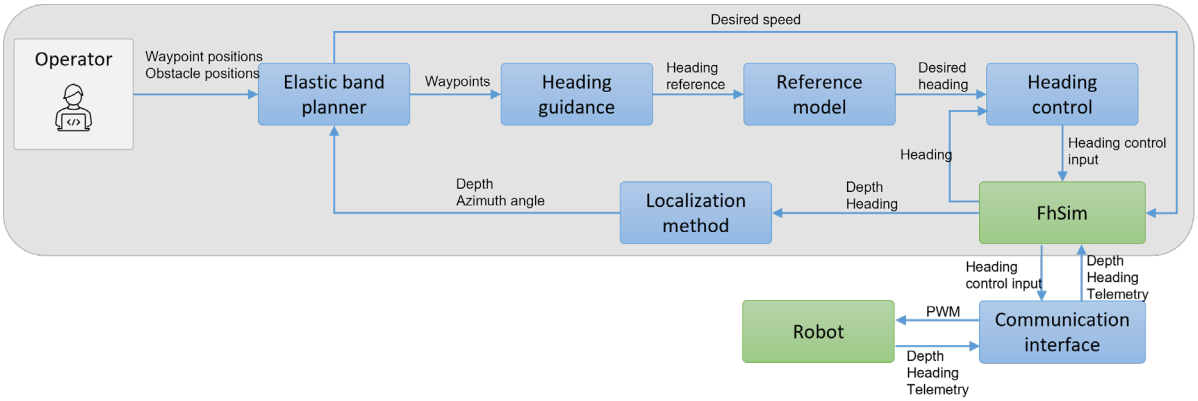

Fig. 2: Block diagram of the overall navigation, guidance and control system.

where $\tilde{\alpha} = \alpha - \alpha_r$ is the azimuth angle error between the vehicle and the next waypoint and $\tilde{D} = D - D_r$ is the depth error between the vehicle and the next waypoint. α_r and D_r are the azimuth reference angle and the depth reference, respectively, for the next waypoint.

III. Experimental Setup and Results

The developed system was demonstrated and validated in two distinct case studies. Case study 1 consisted of simulations in FhSim [22], [23], where the robot followed advanced paths while avoiding obstacles to validate the localization method and the adapted elastic band method. FhSim is a SINTEF Ocean hosted simulation software implemented in C++ that offers a large collection of numerical models relevant to aquaculture operations, including net pens, underwater vehicles, and fish behaviour [22]. Case study 2 consisted of field trials where the system was tested on the Remora robot [7], and heading control and collision avoidance using the adapted elastic band method were verified at sea in an industrial net pen.

A. Case Study 1 - Simulations in FhSim

The localization method, (9)-(13), uses the depth and heading measurements from the mathematical model (1) as input. The depth and heading measurements are exact values with added Gaussian noise of zero mean and standard deviation of $\sigma_D = 0.02$ and $\sigma_\psi = 0.017$ for depth and heading, respectively. This yields measurements with an average error of 0.02 m in depth and 0.017 rad (1.0°) in heading, and a 95 % probability that the measurement error is within 0.04 m and 0.034 rad (2.0°) in depth and heading, respectively. The output from the elastic band path planner is the position of the next waypoint which is given to the guidance model that calculates a reference heading for the robotic system. The reference heading is further fed into the heading controller which calculates the desired output thrust. A block diagram of the overall navigation, guidance and control system is presented in Figure 2. The blocks not included in the grey area are only applicable for field trials when an external robot is considered.

The heading controller in the simulations is an angular rate controller that controls the yaw rate. The desired yaw rate can be calculated by using

$$\dot{\psi}_d = -K\tilde{\psi}, \tag{16}$$

where $K > 0$ is a gain metric and $\tilde{\psi}$ is the yaw error given by

$$\tilde{\psi} = \psi - \psi_r. \tag{17}$$

Here, ψ_r is the reference heading outputted from the heading guidance (15) and ψ is the heading of the robotic system. Furthermore, the yaw rate error is found with

$$\dot{\tilde{\psi}} = \dot{\psi} - \dot{\psi}_d, \tag{18}$$

and the control law is then derived as a proportional controller with

$$\tau_r = -K_p\tilde{\psi}, \tag{19}$$

where $K_p > 0$ is the proportional gain and τ_r is the desired thrust moment in yaw.

The surge speed controller is a sigmoid function with the form

$$\tau_u = -\delta + K_u \frac{1}{1 + e^{-K_s u_d}}, \tag{20}$$

where δ is an offset, K_u is a controller gain and K_s is the sigmoid gain. This way, τ_u will be mapped between $-\delta \quad K_u - \delta$.

The heading controller and surge speed controller are applied alongside the elastic band path planner, heading guidance, and localization method in FhSim. In the simulations, the robotic system should move in a vertical lawn mower pattern [24]–[26] in a cylindrical net pen, while simultaneously avoiding obstacles in its path. The parameters for the simulation results presented in this section are given in Table I, where the waypoint parameters are calculated by

$$N_W = \left(\frac{4\pi r}{I_W} + 2\right)\frac{N_Q}{4} \tag{21}$$

$$W_{i,a} = floor\left(\frac{i}{2}\right)\frac{I_W}{r_c^*} \tag{22}$$

$$W_{i,D} = \begin{cases} 0 & \text{if } remainder(\frac{i}{4}) = 0 \\ 13 & \text{if } remainder(\frac{i}{4}) = 1 \\ 15 & \text{if } remainder(\frac{i}{4}) = 2 \\ 2 & \text{if } remainder(\frac{i}{4}) = \end{cases} \quad (23)$$

TABLE I: Simulation parameters

Parameter	Value	Description
K	1.0	Desired yaw rate gain metric.
K_p	1.0	Heading controller proportional gain.
δ	2.0	thrust offset in the surge speed controller.
K_u	4	Surge speed controller gain.
K_s	15	Sigmoid gain in the surge speed controller.
Δ	4 [m]	Lookahead-distance.
r_c^*	24.4 [m]	Radius of the net pen.
N_W	from (21)	Number of waypoints calculated from (21).
$W_{i,a}$	from (22)	Azimuth angle of waypoint i calculated from (22).
$W_{i,D}$	from (23)	Depth of waypoint i calculated from (23).
I_W	3 [m]	Spacing between two consecutive straight paths in the lawn mower pattern. Also referred to as pitch in the literature.
N_Q	2	Number of quadrants the robot should clean.
N_O	10	Set the number of obstacles.
O_1	[0.5, 8, 0.9]	Azimuth angle, depth, radius of Obstacle 1.
O_2	[1.0, 11, 0.9]	Azimuth angle, depth, radius of Obstacle 2.
O_3	[1.0, 4, 0.9]	Azimuth angle, depth, radius of Obstacle 3.
O_4	[1.4, 9, 0.9]	Azimuth angle, depth, radius of Obstacle 4.
O_5	[1.8, 8, 0.9]	Azimuth angle, depth radius of Obstacle 5.
O_6	[2.2, 8, 0.9]	Azimuth angle, depth, radius of Obstacle 6.
O_7	[2.5, 4, 0.9]	Azimuth angle, depth, radius of Obstacle 7.
O_8	[2.8, 8, 0.9]	Azimuth angle, depth, radius of Obstacle 8.
O_9	[3.0, 2, 0.9]	Azimuth angle, depth, radius of Obstacle 9.
O_{10}	[3.2, 9, 0.9]	Azimuth angle, depth, radius of Obstacle 10.

With the parameters set as in Table I, Figure 3a plots the trajectory of the robotic system during simulation where the blue line is the trajectory and the red circles are obstacles. Furthermore, Figure 3b plots the distance between the robot and the closest obstacle, where the red line represents the sum of the obstacle radius, the minimum bubble radius from the elastic band method, and a safety margin distance. During the simulations, the distance to the object never crossed this line, which demonstrated that the robot was able to keep a safe distance from all obstacles at all times.

The robotic system was able to follow the vertical lawn mower pattern, while simultaneously avoiding the obstacles in its path. Furthermore, Figure 4 plots the azimuth angle error during the simulation. The maximum azimuth error appeared at t = 365 seconds and was 0.0067 radians (0.38°). The root mean square error (RMSE) was 0.0028 radians (0.16°). Considering that the cage radius in the simulation was r_c^* = 24.4 m, the maximum azimuth angle error was equivalent to an arc length of 0.162 m and the equivalent RMSE arc length was 0.068 m. The maximum arc length error was within the safety margin distance set in the elastic band method, and the results were thus deemed satisfactory.

B. Case study 2 - Field trials in a net pen

Case study 2 involved the net crawling robot Remora from Remora Robotics [7], shown in Figure 5. The robot was placed in a net pen and controlled from an onshore control room using remote control. The remote control interface was enabled through Transmission Control Protocol/Internet Protocol (TCP/IP) communication over 4G network. A communication interface was set up with the MAVLink messaging protocol [27] to convert control inputs to pulse-width modulation (PWM) signals that were sent to the robot, and to receive and translate information from the robot such as depth, heading and telemetry measurements.

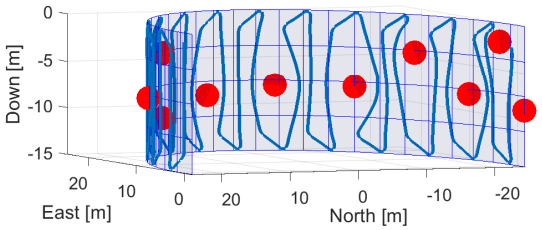

(a) North, East, Down positions of the robot during simulation. The blue line is the trajectory of the robot and the red dots are obstacles. The robot follows a vertical lawnmower pattern while avoiding the obstacles.

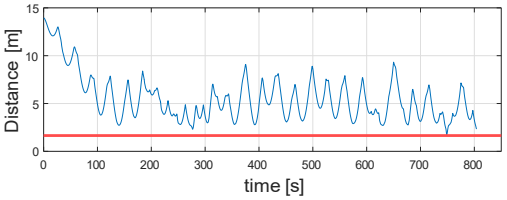

(b) The distance between the robot and the closest obstacle. The red line represents the obstacle radius + safety margin + minimum bubble radius.

Fig. 3: Simulation results.

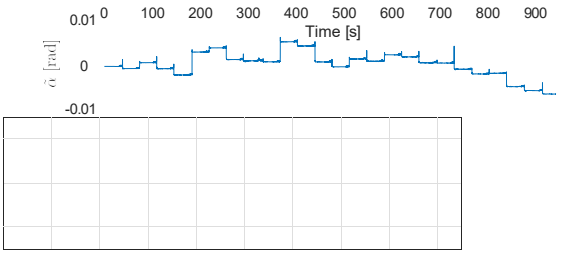

Fig. 4: The error of the estimated azimuth angle compared to the true value during simulation given by $\bar{\alpha} = \hat{\alpha} - \alpha$, where $\hat{\alpha}$ is the estimated azimuth angle and α is the true value.

Fig. 5: The Remora cleaning robot. Image courtesy of Remora Robotics [7].

Case study 2 involved the same navigation and guidance

system as in Case study 1; however the heading control, surge control, and robotic interface differed. In Case study 2, a reference model [17, Ch. 10.2] was included to ensure a smooth trajectory and to avoid rapid turns. Furthermore, the heading controller was changed to a proportional-integral (PI) controller, where the integral term was included to eliminate residual error. The PI-controller has the form

$$\tau_r = -K_p\tilde{\psi} - K_i \int_0^t \tilde{\psi}(\tau)d\tau, \quad (24)$$

where $K_p > 0$ and $K_i > 0$ are proportional and integral gain, respectively, and $\tilde{\psi}$ is the heading angle error computed from

$$\tilde{\psi} = \psi - \psi_d \quad (25)$$

Here, ψ_d is the filtered reference heading from the reference model (see more info in [17, Ch. 10.2]), referred to as the desired heading. The surge speed controller directly maps the desired surge speed, u_d, to PWM signals by

$$\tau_u = \delta + \frac{PWM_{max} - PWM_{min}}{u_{max} - u_{min}} \quad (26)$$

where δ is the PWM offset from equilibrium, PWM_{max} and PWM_{min} are the maximum and minimum PWM signals, respectively, and u_{max} and u_{min} are the maximum and minimum surge speed, respectively. The parameters for the results presented in this section are given in Table II. As opposed to the simulations where the waypoints are calculated by (21), (22) and (23), the waypoints for the field trials were manually defined by the authors.

TABLE II: Field trial parameters

Parameter	Value	Description
K_p	0.2	Heading controller proportional gain.
K_i	0.01	Heading controller integral gain.
δ	1500	PWM equilibrium (equals zero surge speed).
PWM_{max}	1900	Maximum PWM signal.
PWM_{min}	1100	Minimum PWM signal.
u_{max}	3.0	Maximum surge speed (m/s).
u_{min}	-3.0	Minimum surge speed (m/s).
Δ	4 [m]	Lookahead-distance.
r	24.4 [m]	Radius of the net pen.
N_W	3	Number of waypoints.
W_1	[0, 7]	Azimuth angle and depth of waypoint 1.
W_2	[0, 12]	Azimuth angle and depth of waypoint 2.
W_3	[0, 15]	Azimuth angle and depth of waypoint 3.
N_O	1	Set the number of obstacles.
O_1	[0.01, 9, 0.1]	Azimuth angle, depth, radius of obstacle 1.

The full navigation, guidance and control system is presented in the block diagram in Figure 2. The blocks outside the grey area should now be considered. Case study 2 involved one main objective and two secondary objectives. The main objective was the validation of the elastic band path planner using the Remora robot in the net pen. The two secondary objectives included validating the heading controller and validating the localization method. The validation of the two secondary objectives was important in order to achieve the main objective, and hence they were executed first.

The heading controller was validated with the controller gains listed in Table II. Figure 6 plots the heading of the robot versus the desired heading during validation. The heading angle tracked the desired heading angle with small deviations. The maximum heading angle error was measured to 0.08 radians (4.6°). This nominal performance was considered good enough for the heading controller to be used with the elastic band planner. Further tuning of the control gains could be targeted in the future if more precision is required for more complex operations.

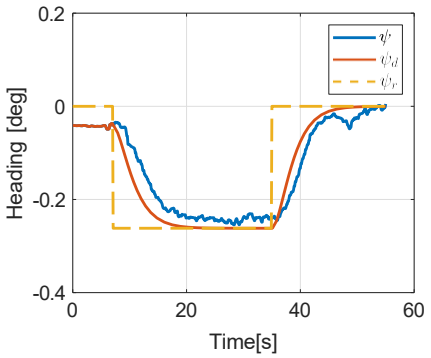

Fig. 6: Validation of the heading control. ψ is the heading, ψ_d the desired heading, and ψ_r the unfiltered heading reference provided by the pure pursuit guidance model.

The localization method was validated to ensure that the azimuth angle demonstrated reasonable behaviour. It should be noted that there was no ground truth measurement of this variable. Hence, there was no unambiguous way of verifying the estimated position and the objective opinion of the operators was used for validation. The signal quality was considered important, and, as can be seen in Figure 7, t e localization method provided a signal with very low r ise levels and the signal reflected the path observed by the erators during the trial. The estimator was thus considered s ited for use with the elastic band method.

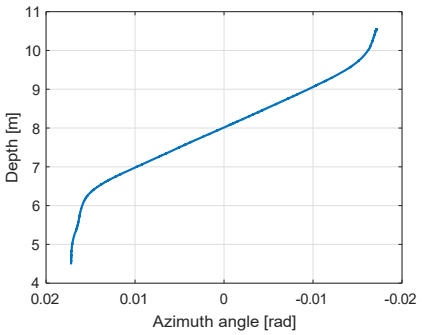

Fig. 7: Validation of the localization method.

The elastic band method was validated by considering three waypoints in a straight line and a virtual obstacle in the shape of a sphere with radius 0.1 m. The positions of the waypoints and the obstacle are listed in Table II.

Figures 8 and 9 plot snapshots of the field trial at different time instances. From Figure 8, it can be seen that the elastic band method generated a path with respect to the safety margin of the obstacle and ensured that the robot was within

the free space the whole time. The bubbles along the elastic band are subsets of the free space, and they could vary between 0.5–1.5 m. In order to guarantee that the area inside the bubbles could be considered a safe space at all times, the minimum radii of these bubbles were chosen to be larger than the radius of the vehicle. In addition, the safety margin parameter added an extra space between the bubbles and the obstacle to ensure that the vehicle avoided the obstacle. The elastic band method dynamically altered the size of the bubbles and the desired vehicle speed based on the distance to the object. As seen in Figure 8, the size of the bubbles close to the obstacle was smaller than the bubbles further away, and consequently, the desired speed was lower (14). As follows, the trajectory of the robot is more rigid and precise which contributes to preventing collisions. Finally, Figure 9 shows how the robot was able to reach the individual waypoints while simultaneously avoiding the obstacle, and Figure 10 shows that the implemented heading controller ensured that the robot was able to follow the desired heading trajectory generated by the elastic band method and the reference model with only small deviations during sharp turns.

When using dead reckoning for localization it is known that more intricate experiments over longer periods of time will result in more accumulated error over time. This was not deemed a problem in these results since the duration of the experiments were sufficiently short. However, ways of mitigating this error should be investigated for future operations, where perhaps Kalman filters or introducing acoustic measurements to update the estimates could bring good solutions.

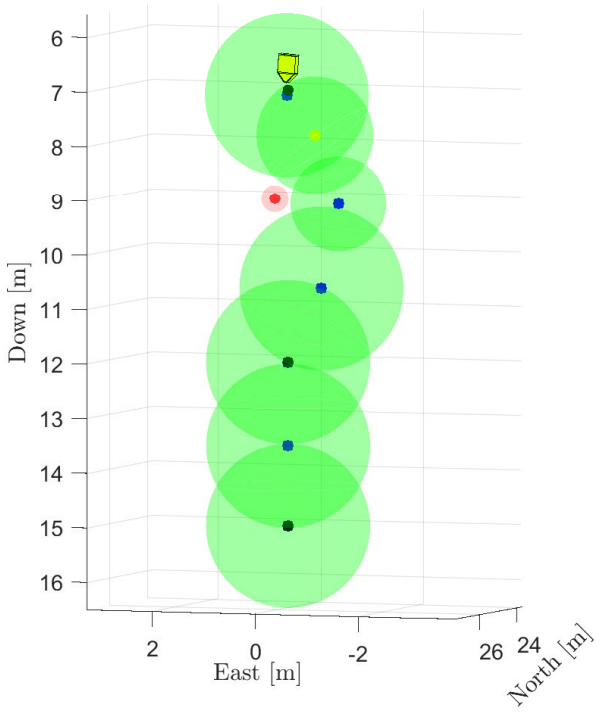

Fig. 8: Snapshot of the experiment at t=10. The robotic system is demonstrated as the yellow vehicle, waypoints as black dots, intermediate waypoints as blue dots, the obstacle as the red dot with the safety margin as the lighter hue around it, and the elastic band bubbles in green.

IV. Conclusions and Future work

This paper developed and demonstrated methods for autonomous operation of net grooming robots in aquaculture net pens. In particular, a localization method for net-crawling robots, a 3 DOF cylindrical robotic model, an elastic band method for path planning and collision avoidance, and a heading guidance and control system are presented and validated in both simulations and field trials. The developed localization method produced estimates with low noise, and through the simulations and field work it was shown that the localization method was able to estimate the position of the robot in the net pen with sufficient accuracy using only heading and depth measurements. In addition, the validations showed that the robotic system avoided obstacles while reaching the desired waypoints. Thus, this work successfully demonstrated that the presented system is applicable for path planning and collision avoidance for net crawling robots, and contributes to enabling uninterrupted operation for grooming robots in the aquaculture industry. Future work includes validation of the methods in more intricate experiments involving complex paths and dynamic obstacles. In addition, methods for dynamic detection of obstacles should be investigated.

Acknowledgment

This work was funded by the Research Council of Norway (RCN) through the projects: NetClean 24/7 (RCN project no. 296392) and CHANGE (RCN project no. 313737). The authors would like to thank Remora Robotics, the project owner of the NetClean24/7-project, for their support before and during the field trials.

References

[1] J. Bannister, M. Sievers, F. Bush, and N. Bloecher, "Biofouling in marine aquaculture: a review of recent research and developments," *Biofouling*, vol. 35, no. 6, pp. 631–648, 2019.

[2] I. Fitridge, T. Dempster, J. Guenther, and R. de Nys, "The impact and control of biofouling in marine aquaculture: a review," *Biofouling*, vol. 28, no. 7, pp. 649–669, 2012.

[3] N. Bloecher, M. Powell, S. Hytterød, M. Gjessing, J. Wiik-Nielsen, S. N. Mohammad, J. Johansen, H. Hansen, O. Floerl, and A.-G. Gjevre, "Effects of cnidarian biofouling on salmon gill health and development of amoebic gill disease," *PLOS ONE*, vol. 13, pp. 1–18, 07 2018.

[4] N. Bloecher, K. Frank, M. Bondø, D. Ribicic, P. C. Endresen, B. Su, and O. Floerl, "Testing of novel net cleaning technologies for finfish aquaculture," *Biofouling*, vol. 35, no. 7, pp. 805–817, 2019.

[5] T. Thorvaldsen, T. Kongsvik, I. M. Holmen, K. Størkersen, C. Salomonsen, M. Sandsund, and H. V. Bjelland, "Occupational health, safety and work environments in Norwegian fish farming - employee perspective," *Aquaculture*, vol. 524, p. 735238, 2020.

[6] T. Thorvaldsen, K. Størkersen, T. Kongsvik, and I. M. Holmen, "Safety management in Norwegian fish farming: Current status, challenges, and further improvements," *Safety and Health at Work*, vol. 12, no. 1, pp. 28–34, 2021.

[7] Remora Robotics, "A robot that cleans and inspects fish pens while collecting data." https://remorarobotics.no/autonomous-cleaning-robot/, 2022. [Online; accessed 07-November-2022].

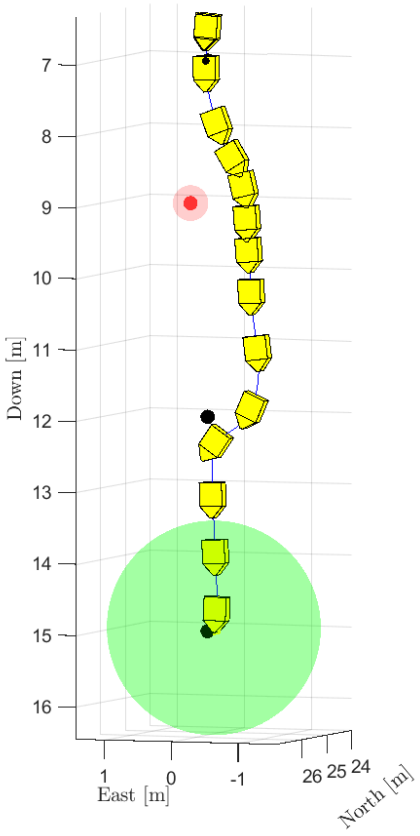

Fig. 9: Snapshot of the experiment at the end.

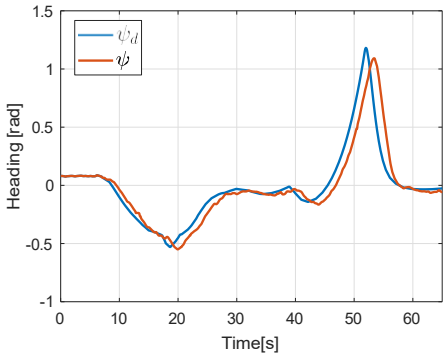

Fig. 10: The desired heading angle and the measured heading angle during an experiment.

[8] N. Bloecher and O. Floerl, "Towards cost-effective biofouling management in salmon aquaculture: a strategic outlook," *Reviews in Aquaculture*, vol. 13, no. 2, pp. 783–795, 2021.

[9] G. Swain, C. Erdogan, L. Foy, H. Gardner, M. Harper, J. Hearin, K. Z. Hunsucker, J. T. Hunsucker, K. Lieberman, M. Nanney, E. Ralston, A. Stephens, M. Tribou, B. Walker, and A. Wassick, "Proactive in-water ship hull grooming as a method to reduce the environmental footprint of ships," *Frontiers in Marine Science*, vol. 8, 2022.

[10] S. J. Ohrem, E. Kelasidi, and N. Bloecher, "Analysis of a novel autonomous underwater robot for biofouling prevention and inspection in fish farms," in *2020 28th Mediterranean Conference on Control and Automation (MED)*, pp. 1002–1008, 2020.

[11] S. J. Ohrem, H. B. Amundsen, and E. Kelasidi, "Control-oriented modeling of an underwater biofouling prevention robot," in *2021 20th International Conference on Advanced Robotics (ICAR)*, pp. 1121–1128, 2021.

[12] J. Bao, D. Li, X. Qiao, and T. Rauschenbach, "Integrated navigation for autonomous underwater vehicles in aquaculture: A review," *Information Processing in Agriculture*, vol. 7, no. 1, pp. 139–151, 2020.

[13] J. DeCew, D. Fredriksson, P. Lader, M. Chambers, W. Howell, M. Osienki, B. Celikkol, K. Frank, and E. Høy, "Field measurements of cage deformation using acoustic sensors," *Aquacultural Engineering*, vol. 57, pp. 114–125, 2013.

[14] P. Klebert, Øystein Patursson, P. C. Endresen, P. Rundtop, J. Birkevold, and H. W. Rasmussen, "Three-dimensional deformation of a large circular flexible sea cage in high currents: Field experiment and modeling," *Ocean Engineering*, vol. 104, pp. 511–520, 2015.

[15] S. Quinlan and O. Khatib, "Elastic bands: connecting path planning and control," in *Proc. IEEE International Conference on Robotics and Automation*, pp. 802–807, 1993.

[16] M. Føre, S. Fjæra, S. J. Ohrem, E. Kelasidi, N. Bloecher, and H. B. Amundsen, "Adaptive motion planning and path following for permanent resident biofouling prevention robot operating in fish farms," in *OCEANS 2021: San Diego – Porto*, pp. 1–10, 2021.

[17] T. I. Fossen, *Handbook of Marine Craft Hydrodynamics and Motion Control*. John Wiley & Sons, Ltd., 2011.

[18] H. B. Amundsen, W. Caharija, and K. Y. Pettersen, "Autonomous ROV inspections of aquaculture net pens using DVL," *IEEE Journal of Oceanic Engineering*, vol. 47, no. 1, pp. 1–19, 2022.

[19] M. Bjerkeng, T. Kirkhus, W. Caharija, J. T. Thielemann, H. B. Amundsen, S. Johan Ohrem, and E. Ingar Grøtli, "ROV navigation in a fish cage with laser-camera triangulation," *Journal of Marine Science and Engineering*, vol. 9, no. 1, 2021.

[20] P. Rundtop and K. Frank, "Experimental evaluation of hydroacoustic instruments for ROV navigation along aquaculture net pens," *Aquacultural Engineering*, vol. 74, pp. 143–156, 2016.

[21] E. Kelasidi, B. Su, W. Caharija, M. Føre, M. Pedersen, and K. Frank, "Autonomous monitoring and inspection operations with UUVs in fish farms," *IFAC-PapersOnLine*, vol. 55, no. 31, pp. 401–408, 2022. 14th IFAC Conference on Control Applications in Marine Systems, Robotics, and Vehicles CAMS 2022.

[22] K.-J. Reite, M. Føre, K. Aarsæther, J. Jensen, P. Rundtop, L. Kyllingstad, P. Endresen, D. Kristiansen, V. Johansen, and A. Fredheim, "FHSIM — time domain simulation of marine systems," *Proceedings of the International Conference on Offshore Mechanics and Arctic Engineering - OMAE*, vol. 8, 06 2014.

[23] B. Su, K.-J. Reite, M. Føre, K. G. Aarsæther, M. O. Alver, P. C. Endresen, D. Kristiansen, J. Haugen, W. Caharija, and A. Tsarau, "A multipurpose framework for modelling and simulation of marine aquaculture systems," vol. Volume 6: Ocean Space Utilization of *International Conference on Offshore Mechanics and Arctic Engineering*, 06 2019.

[24] J. Ousingsawat and M. G. Earl, "Modified lawn-mower search pattern for areas comprised of weighted regions," in *2007 American Control Conference*, pp. 918–923, 2007.

[25] J. Frost, *Principles of search theory*. 2000.

[26] A. D. Ryan, D. L. Nguyen, and J. K. Hedrick, "Hybrid Control for UAV-Assisted Search and Rescue," vol. Dynamic Systems and Control, Parts A and B of *ASME International Mechanical Engineering Congress and Exposition*, pp. 187–195, 11 2005.

[27] A. Kouba˙a, A. Allouch, M. Alajlan, Y. Javed, A. Belghith, and M. Khalgui, "Micro air vehicle link (MAVlink) in a nutshell: A survey," *IEEE Access*, vol. 7, pp. 87658–87680, 2019.